On-Demand Electrochemical Fabrication of Ordered Nanoparticle Arrays using Scanning Electrochemical Cell Microscopy

*Md. Maksudur Rahman,[1] Chloe L. Tolbert,[1] Partha Saha,[1] Jeffrey Halpern,[2] and Caleb M. Hill[1]**

[1]Department of Chemistry, University of Wyoming 1000 East University Avenue, Laramie, Wyoming 82071, USA

[2]Department of Chemical Engineering and the Materials Science and Engineering Program, University of New Hampshire, 33 Academic Way, Durham, NH 03824, USA

ABSTRACT. Well-ordered nanoparticle arrays are attractive platforms for a variety of analytical applications, but the fabrication of such arrays is generally challenging. Here, it is demonstrated that Scanning Electrochemical Cell Microscopy (SECCM) can be used as a powerful, instantly reconfigurable tool for the fabrication of ordered nanoparticle arrays. Using SECCM, Ag nanoparticle arrays were straightforwardly fabricated via electrodeposition at the interface between a substrate electrode and an electrolyte-filled pipet. By dynamically monitoring the currents flowing in an SECCM cell, individual nucleation and growth events could be detected and controlled to yield individual nanoparticles of controlled size. Characterization of the resulting arrays demonstrate that this SECCM-based approach enables spatial control of nanoparticle location comparable with the terminal diameter of the pipet employed and straightforward control over the volume of material deposited at each site within an array. These results provide further

evidence for the utility of probe-based electrochemical techniques such as SECCM as tools for surface modification in addition to analysis.

KEYWORDS. Nanoparticles, SECCM, Electrodeposition, Arrays, Nanofabrication

Introduction

The distinctive plasmonic, catalytic, chemical, optical, and electronic properties of nanoparticles (NPs) make them attractive platforms for a variety of sensing technologies.[1–7] In most practical applications, NPs must be immobilized on substrates to perform effectively, but commonly employed attachment methods such as dropcasting or spincoating often yield random, disordered films.[8,9] The random nature of these films has a negative impact on reproducibility due to NP-to-NP variations in surface accessibility or optical properties arising from interparticle coupling.[10–13]

Well-ordered arrays of NPs retain the favorable properties of NPs for sensing applications while minimizing the reproducibility issues associated with randomly fabricated surfaces. Their fabrication is not trivial, however, and most approaches reported to date require expensive lithographic techniques like optical printing,[14,15] plasma etching,[16] photo lithography,[17] self-assembly,[18,19] electron beam lithography,[20] atomic layer deposition,[21–23] soft lithography,[24,25] nano sphere lithography,[26] nano imprint lithography,[27–30] and scanning probe lithography.[31] Here, we demonstrate that Scanning Electrochemical Cell Microscopy (SECCM)[32–38] can be utilized to form well-ordered NP arrays in a powerful, instantly reconfigurable manner. In SECCM, electrolyte-filled pipets are utilized to define nm-scale electrochemical interfaces which enable the high-resolution analysis of chemical processes spanning electrocatalysis,[39–44] anodic dissolution,[45,46] photoelectrochemistry,[47–52] ionic transport,[53] and crystallization.[54]

Here, SECCM was utilized to synthesize ordered arrays of isolated Ag NPs via electrodeposition from pipets containing metal salt precursors. Direct growth is considered more reproducible and

stable compared to more commonly employed drop-casting methods,[8] and the use of SECCM allows the localized direct growth of nanoparticles in a controlled manner for patterning. While NP synthesis is known to follow a stochastic nucleation and growth process, the reproducible synthesis of individual NPs of controlled size via SECCM was enabled by controlling the charge flowing during an individual synthesis event. The kinetics and spatial control of the growth process were analyzed as a function of applied potential, and finite element simulations were carried out to provide theoretical context for these observations. These results demonstrate SECCM can be straightforwardly adapted as a powerful tool for on-demand nanofabrication for a variety of potential applications.

Results and Discussion

NP Array Synthesis via SECCM. The NP array fabrication strategy employed in these experiments is illustrated in **Figure 1**. A pipet with sub-micron terminal dimensions was prepared via laser-based pipet pulling, filled with an electrolyte solution containing a metal precursor ($AgNO_3$ in the present experiments), and a metal wire (Ag) was inserted to complete the probe. The Ag wire served as a quasireference-counter electrode (QRCE), its potential set by the Ag^+/Ag redox couple.

The probe was brought into contact with a sample substrate (indium tin oxide, ITO), creating a miniaturized electrochemical cell where the working electrode surface is defined by the electrolyte-substrate interface. A cathodic potential could then be applied to drive the reduction of Ag^+ ions to Ag on the substrate surface:

$$\mathrm{Ag}^{+}_{(\mathrm{aq})} + \mathrm{e}^{-} \rightarrow \mathrm{Ag}_{(s)} \qquad 1$$

A cyclic voltammogram depicting Ag electrodeposition at a bulk (0.5 mm diameter) ITO electrode can be found in **Figure 2a**. As potentials are swept towards cathodic potentials, cathodic

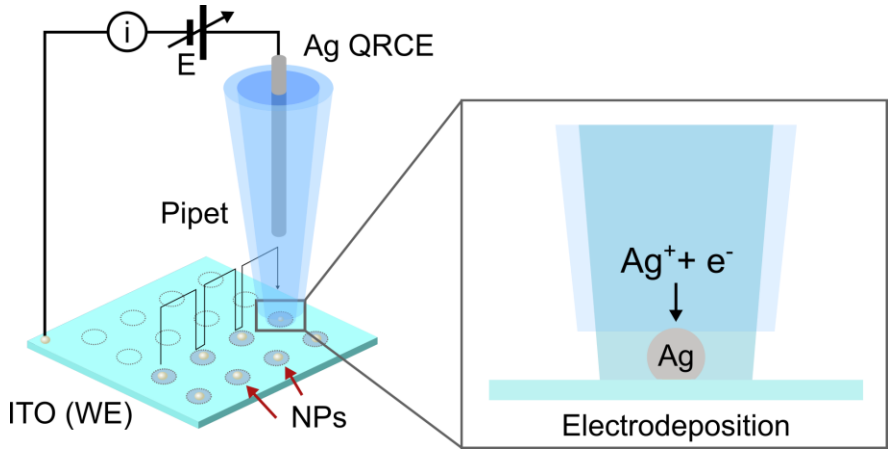

Figure 1. Schematic illustration of nanoparticle array fabrication via scanning electrochemical cell microscopy (SECCM).

currents begin to be observed at ca. -0.2 V vs. Ag^+/Ag, corresponding to the electrodeposition of Ag. During the subsequent anodic sweep, cathodic currents continue to be observed until ca. -0.05 V vs. Ag^+/Ag. This "nucleation loop" is commonly observed in the voltammetry of electrodeposition processes, arising from the larger overpotentials needed to drive the formation of thermodynamically-stable nuclei on the electrode surface than to drive electrodeposition of the bulk material.[55,56] This nucleation-and-growth process will typically involve the formation and growth of millions of individual nuclei across mm^2-scale interfaces.

Here, the ability of SECCM to define electrochemical interfaces with sub-µm dimensions is leveraged to systematically electrodeposit individual metal NPs at desired locations on a substrate. The general approach employed is illustrated in **Figure 2b**. An anodic bias is applied between the ITO substrate and the Ag QRCE while the probe is translated towards the substrate surface. Probe movement is stopped upon observation of an anodic current spike resulting from probe-substrate contact. A cathodic potential is then applied to the ITO substrate, which results in a quickly decaying charging transient. The current flowing through the system is then monitored until another cathodic current transient is observed. This second transient is associated with the nucleation and growth of a NP on the ITO substrate. Because the initial formation of a

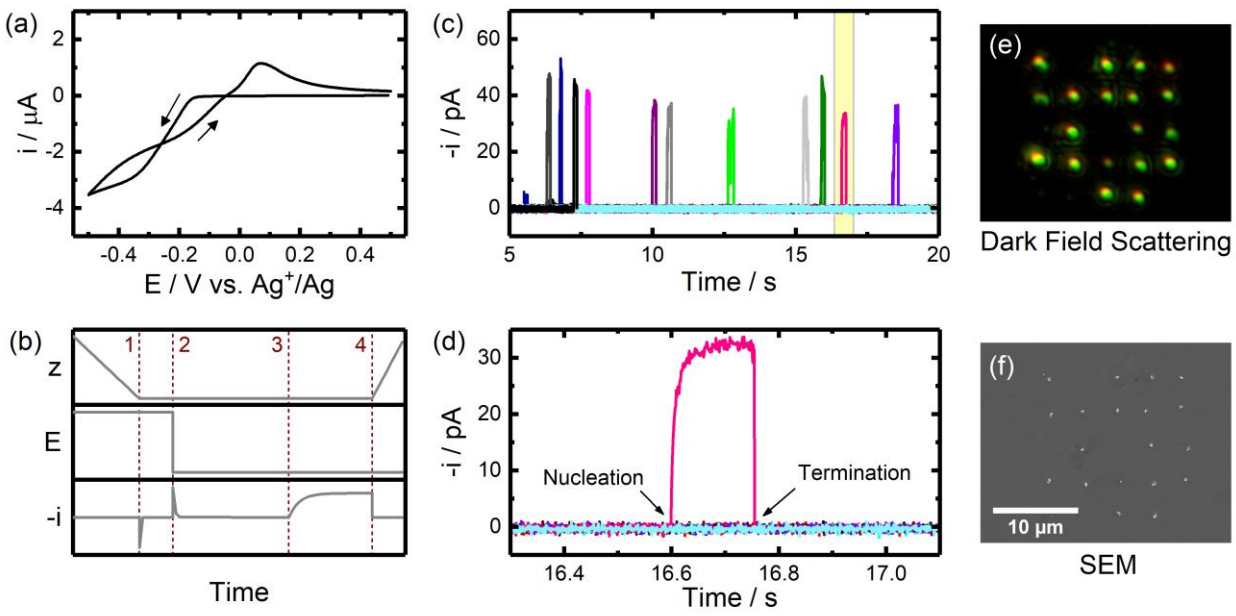

Figure 2. Electrodeposition of Ag NP Arrays. (a) Cyclic voltammogram obtained at a bulk ITO electrode (0.5 mm diameter) in an aqueous solution containing 0.25 mM $AgNO_3$ and 250 mM KNO_3. (b) Schematic depicting the probe position, applied potential, and current during a single deposition cycle. Red dashed lines highlight important events during the cycle: (1) detection of probe-sample contact, (2) application of a cathodic potential, (3) NP nucleation, and (4) probe retraction and growth termination. (c) Example deposition transients observed during array fabrication with 5 pC of charge deposited at each location. Electrodeposition was carried out using a ~1 µm pipette filled with an aqueous solution of 0.25 mM $AgNO_3$ and 0.25 mM KNO_3. Note the negative of the current is plotted for clarity. (d) A magnified view of the transient indicated in (c). Optical and Scanning Electron Microscopy images of the fabricated array are provided in (e) and (f).

thermodynamically stable nuclei is a stochastic process,[57,58] the "waiting time" between the cathodic transients is highly variable from NP-to-NP. Upon nucleation, the current flowing through the SECCM cell can be integrated to track the total charge passed, and therefore volume of material deposited via Faraday's law:

$$V = \frac{V_m Q}{nF} \qquad 2$$

where V_m is the molar volume, Q is the charge passed, n is the number of electrons passed in the reaction, and F is Faraday's constant. Example *i-t* curves obtained during the deposition of a 5 pC (-0.5 V) Ag NP array are provided in **Figure 2c-d**.

As can be seen in **Figure 2c**, there is a large variability in the waiting time required for each deposition event to occur. As described above, this is expected due to the stochastic nature of the

nucleation and growth process and would also be impacted by site-to-site variability in the surface energy of the ITO substrate. A detailed view of an individual deposition transient is given in **Figure 2d**. At short times following nucleation (< 50 ms), the current follows the $t^{1/2}$ dependence expected for the diffusion-limited electrodeposition of NPs on μm-scale electrodes.[59–62] At longer times, however, the transient adopts a steady-state value which results from mass transport limitations imposed by the pipet geometry. A more detailed discussion of these effects are given below. NPs could be visualized at the vast majority of points in the resulting arrays via optical and scanning electron microscopies, clearly confirming the successful electrodeposition of NPs. Missing NPs can be attributed to a lack of nucleation during the finite timescale spent at each location (no deposition transients are observed experimentally at these locations).

Success Rate of NP Fabrication. The probability of successfully synthesizing at least 1 NP at n locations within an array of N points can be described by a binomial distribution:

$$P_n = \frac{N!\, p^n (1-p)^{N-n}}{n!\,(N-n)!} \qquad 3$$

where p is the probability of synthesizing at least 1 particle. If NP nucleation is assumed to be a random, stochastic process describable by a static nucleation rate, k_n, this probability is:

$$p = 1 - e^{-k_n t} \qquad 4$$

where t is the time spent at each point in the array. The number of non-vacant array locations should thus exhibit a sigmoidal dependence on the nucleation rate. This dependence was experimentally interrogated by examining the number of vacant points in arrays fabricated with different applied potentials and typical results are provided in **Figure 3a** (see SI for further discussion and details on error estimation). As can be seen, the number of fabricated NPs exhibited a sigmoidal-type dependence on the applied potential, reflecting an expected increase in nucleation

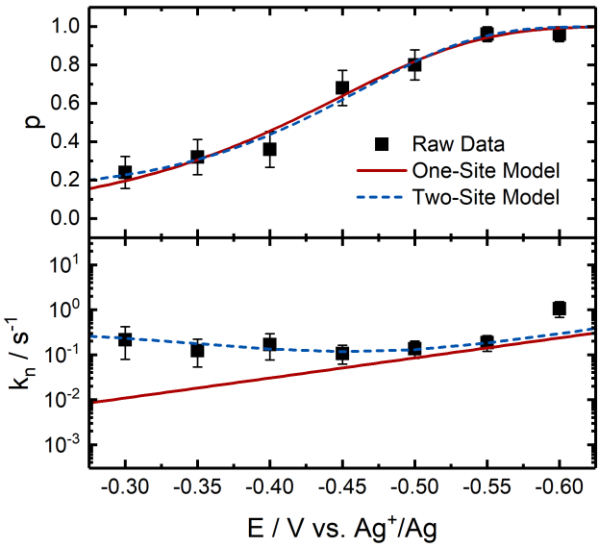

Figure 3. Statistical analysis of nucleation as a function of applied potential. (a) Nucleation probability. (b) Nucleation rate. Data was obtained from the electrodeposition of 25-point Ag NP arrays carried out using a ~1 µm pipette filled with an aqueous solution of 0.25 mM $AgNO_3$ and 0.25 mM KNO_3. Error bars denote 95% confidence intervals and lines represent fits to different nucleation models (see text for details).

rate at increasingly cathodic potentials. This behavior can be explained by assuming a simple Butler-Volmer type expression for the nucleation rate:

$$k_n = k^0 e^{-\frac{\alpha F}{RT}(E-E^0)} \qquad 5$$

The observed nucleation probability can be fit well to this simple model, yielding a k^0 value of 5×10^{-4} s^{-1} and an α of 0.3.

A statistical analysis of the experimentally determined nucleation rate, calculated as the inverse of the average nucleation time, is provided in **Figure 3b**. Surprisingly, the experimental nucleation rate does not vary significantly with applied potential, seemingly at odds with the large potential dependence observed for the probability of NP nucleation discussed above. This behavior suggests that a minority of locations on the ITO surface contain nucleation sites which exhibit fast, yet potential-independent nucleation kinetics. This "two-site" model can quantitatively reproduce the behavior observed experimentally (see SI for further discussion).

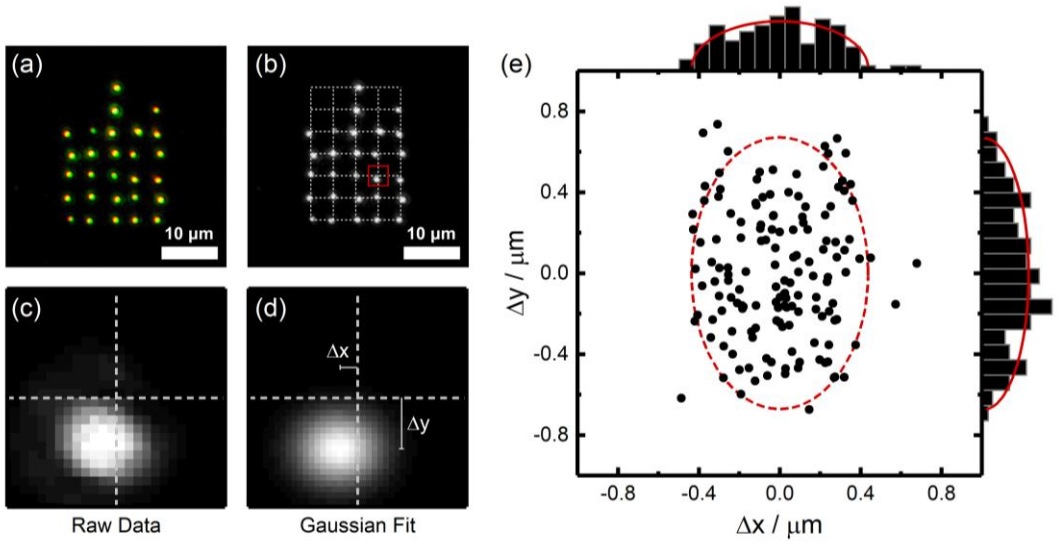

Figure 4. Spatial accuracy of NP electrodeposition. (a) Dark field scattering image of an electrodeposited Ag NP array on ITO. (b) Greyscale image of the same array with grid denoting pipet landing points. (c) Magnified view of scattering profile from an individual Ag NP. (d) 2D Gaussian fit of the same profile used in determining particle offset from pipet landing point. (e) Scatter plot illustrating particle offsets measured for 147 NPs electrodeposited with a single pipet filled with an aqueous solution of 0.25 mM $AgNO_3$ and 0.25 mM KNO_3. Histograms for the observed offsets (Δx, Δy) are also shown with semicircular fits.

Spatial Precision of NP Arrays. The spatial precision of the fabricated NP arrays could play a critical role in practical applications in sensing or catalysis.[8,9] Because NP nucleation will occur at high energy sites within the substrate-electrolyte interface, the geometry of the nm- to µm-scale cell created in SECCM is expected to play a critical role in determining the precision of the resulting NP arrays. To investigate this, optical analyses of fabricated arrays were carried out as illustrated in **Figure 4**. Images of the electrodeposited NP arrays were obtained using dark field imaging. As the deposited NPs are significantly smaller than the diffraction limit of the optical system (~500 nm), individual NPs appear as discrete spots with roughly gaussian intensity profiles. By fitting these profiles to gaussian functions, the spatial locations of individual NPs (taken as the centroid of the gaussian fit) can be determined to a high degree of accuracy (~10 nm).[63–66]

Here, this approach was employed to determine the centroid locations for a series of electrodeposited NPs and the resulting locations were compared to the pipet landing locations

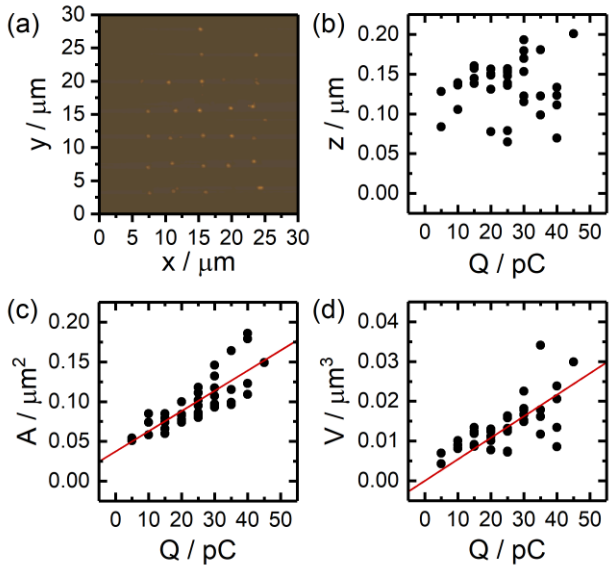

Figure 5. NP Volume Control. (a) AFM image of an electrodeposited Ag NP array on ITO. The charge passed during deposition was varied at each point. (b) NP height, (c) NP area, and (d) NP volume determined from AFM imaging as a function of the deposited charge.

controlled via SECCM (see **Figure 4a-d**). The resulting offsets (Δx and Δy) were determined for >140 NPs deposited with an individual pipet and are plotted in **Figure 4e**. It can be seen that NPs are uniformly distributed across an elliptical area with axes of ~1.0 and ~0.8 µm, which is consistent with the expected meniscus size for the pipets employed in these studies. These results show that NP deposition occurs in a uniform manner across the SECCM interface and probe size is a determining factor in the spatial precision of the fabricated arrays.

NP Geometry Control. The volume of material electrodeposited in a given experiment will be proportional to the charge passed via Faraday's law. As a result, the size of each NP in the SECCM-fabricated arrays described here can be controlled independently by terminating the applied potential once a desired amount of charge has passed. This approach is illustrated in **Figure 5**, which depicts an electrodeposited Ag NP array where the charge passed was varied between 5 and 45 pC. The deposited NPs were characterized using a combination of atomic force microscopy (AFM, **Figure 5a**) and scanning electrochemical microscopy (SEM) and the results are

summarized in **Figure 5b-d**. Interestingly, the height (z) of the deposited NPs did not exhibit a clear relationship with the charge passed, whereas the area exhibited a strong linear relationship. This anisotropic growth behavior may be attributable to preferential mass transport of Ag^+ ions to the ITO-Ag NP interface (*vide supra*).

The volume of the deposited particles exhibited a clear linear relationship with the charge passed with a slope (V_m/nF) of ca. 0.0005 μm^3/pC. This value would correspond to a molar volume of 50 cm^3/mol, which is roughly five times the known value for Ag. This discrepancy suggests the electrodeposited NPs possess a porous structure which lowers their effective density.

Influence of Mass Transport on Deposition Kinetics. Given the fast kinetics of the Ag^+/Ag redox couple,[67] the current transients observed following a nucleation event will be influenced primarily by the mass transfer of Ag^+ ions to the NP surface. The current transient resulting from the diffusion-limited growth of a hemispherical NP is classically described via the following equation:[59,68]

$$i = 2^{3/2}\pi nF(DC^*)^{3/2}V_m^{1/2}t^{1/2} \quad (6)$$

Here, D is the diffusion constant of the NP precursor and C^* is the bulk concentration. The experimental results (see **Figure 2**) shown here deviate from this classical model in two significant ways. First, the transients adopt a steady-state value after a few seconds, which can be attributed to the mass-transport limitations imposed by the SECCM geometry.[50,69] Second, the currents are much larger than those predicted by Eq. 3 on similar timescales. This is due to these experiments being carried out using solutions of relatively low ionic strength to avoid complications related to crystallization, and as a result, the transport of Ag^+ will be impacted to a significant degree by migration.

Finite element simulations were thus employed to model mass transport in these SECCM experiments in order to explain the observed experimental behavior. Two types of NP electrodeposition transients could be identified in these experiments based on their behavior at short timescales, as illustrated in **Figure 6a**. Transients with increasing currents at short timescales were observed in some experiments, while transients with decaying currents at short timescales were observed in others, particularly experiments carried out at more cathodic potentials. To explain these observations, a series of simulations treating the transport of Ag^+ via diffusion and migration in the SECCM geometry were carried out, varying the applied potential vs. the potential of zero charge (E_{pzc}). In these simulations, solutions to the concentration of each ion and the potential were found as a function of time, with a specified potential imposed across the Ag/ITO surface and the concentration of Ag^+ set to 0 at the Ag surface, which was translated based on the local current density to model NP growth (see Supporting Information for more details).

Results from these simulations are summarized in **Figure 6b-d**. When $E = E_{pzc}$, the predicted current transients match those predicted by classical nucleation and growth theory due to the absence of migration effects. At increasing cathodic potentials, however, the currents increase in magnitude and the behavior at short timescales changes drastically, shifting from the traditional $t^{1/2}$-type behavior to transients which initially decay to a steady-state value. These changes can be attributed to the increased impact of migration-driven transport in the system. Further insights can be drawn from the Ag^+ concentration and potential profiles depicted in **Figure 6c**. At this potential ($E - E_{pzc}$ = -0.2 V), the double layer formed near the electrode surface results in an interesting concentration profile, wherein Ag^+ is depleted in the immediate vicinity of the NP but is present at high concentrations near the substrate surface. Even so, these simulations did not predict significant deviations from a traditional hemispherical geometry would occur under these

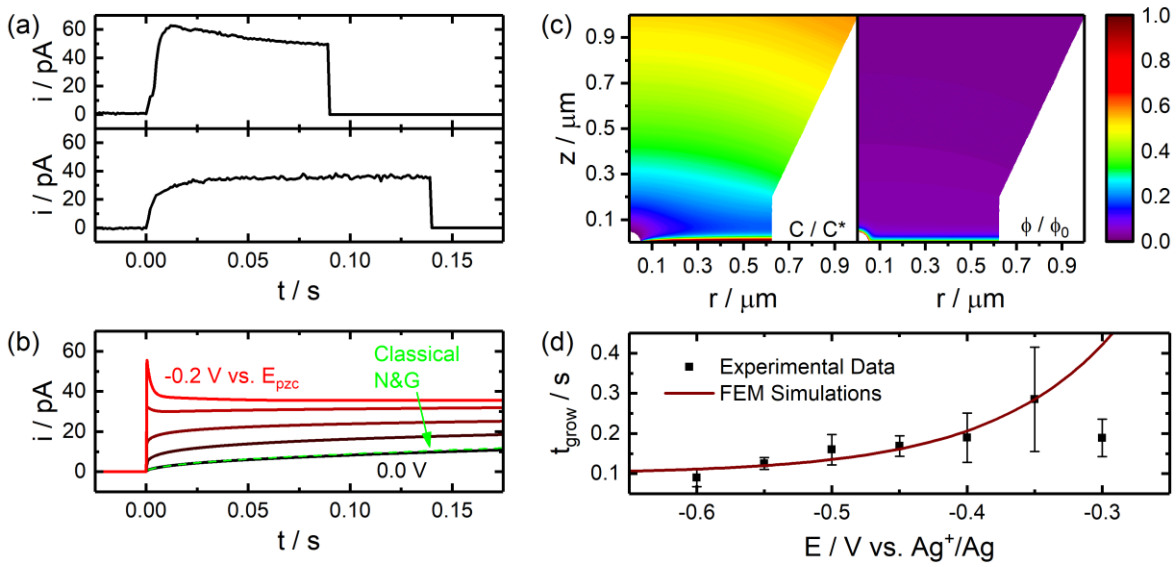

Figure 6. Analysis of current transient profiles in the SECCM geometry. (a) Example current transients observed for the electrodeposition of individual Ag NPs with differing profiles. (b) Simulated current transients from finite element simulations of NP electrodeposition in the SECCM geometry. Simulations were carried out at different applied potentials with respect to the potential of zero charge (E_{pzc}), ranging from 0.0 V (black) to -0.2 V (red) in 50 mV increments. Simulations were carried out for a 1.3 µm diameter pipet filled with an aqueous solution containing 0.25 mM $AgNO_3$ and 0.25 mM KNO_3. All diffusion constants were assumed to be 1.6 x 10^{-5} cm^2 s^{-1}. More details are provided in the SI. (c) Normalized Ag^+ concentration profile and potential profile at t = 0.1 s from the FEM simulations for an applied potential of -0.2 V vs. E_{pzc}. C* denotes the bulk concentration of 0.25 mM and ϕ_0 the potential at the electrode interface, -0.2 V. (d) Comparison of predicted and experimental growth times for particles electrodeposited using a total charge of 5 pC.

conditions (see SI). These simulations were quantitatively compared to experimental results by calculating the time necessary to pass 5 pC of charge, mimicking the experiments depicted in **Figure 2** above. As seen in **Figure 6d**, these simulations reach good agreement with the experimental data, where shorter growth times are observed for increasing cathodic potentials between potential ranges of ca. -0.35 and -0.6 V vs. Ag^+/Ag (the discrepancy observed at -0.3 V is likely attributable to poor statistics due to the low likelihood of nucleation).

On-Demand Electrodeposition of Complex Array Patterns. A major potential advantage of SECCM for NP array fabrication is the on-demand nature with which complex array patterns can be generated, not achievable using conventional lithographic techniques. This flexibility is demonstrated in **Figure 7**, which includes optical and scanning electron microscopy images of Ag NP arrays fabricated in well-defined patterns. Such patterns can be incorporated in a relatively

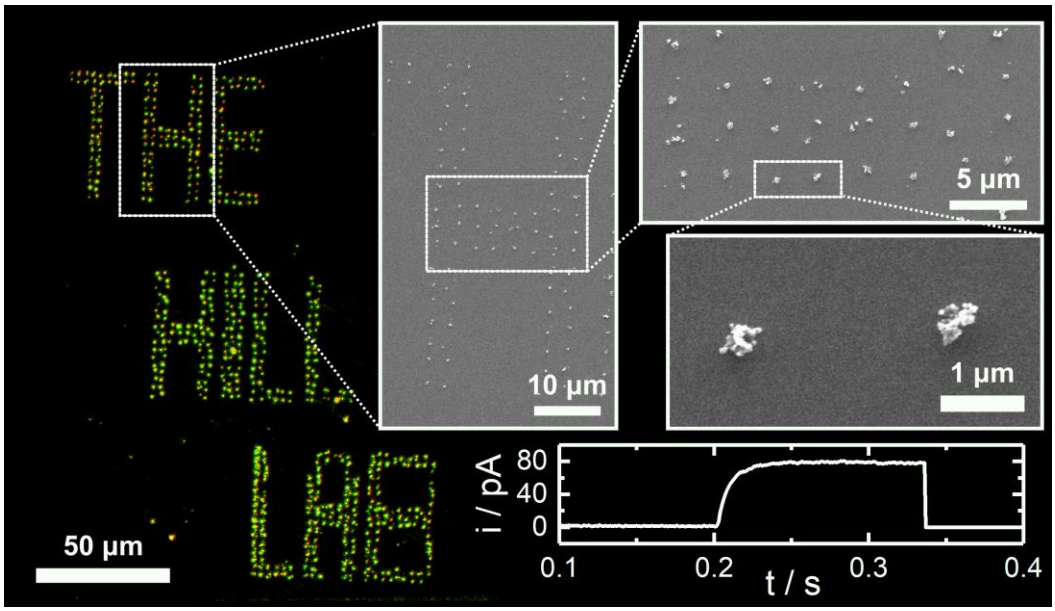

Figure 7. Generating Complex Array Patterns via SECCM. Optical dark field scattering and scanning electron microscopy images of Ag NP arrays on ITO substrates fabricated via SECCM. Electrodeposition was carried out using a ~1 µm pipette filled with an aqueous solution of 0.25 mM $AgNO_3$ and 0.25 mM KNO_3, passing 10 pC of cathodic charge while holding the ITO potential at -0.5 V vs. Ag^+/Ag.

trivial manner, requiring only an additional numerical array to be included as an input to the instrumental control software which contains the charge to be deposited at each point. These results demonstrate the high reproducibility of this approach, enabling 100's of individual NPs to be fabricated in succession without the fouling of probes. A current limitation, however, is the non-ideal, fractal-like NP geometry obtained in some cases (see SEM images in **Figure 7**). Experiments are currently underway to address this issue by controlling the electrolyte chemistry utilized for deposition.

Conclusions

In this report, the fabrication of well-ordered arrays of metal NPs using SECCM was demonstrated. By actively monitoring the currents flowing in small, nm- to µm-scale electrochemical cells, individual NPs can be reproducibly synthesized in an on-demand fashion via electrodeposition. This approach enables high degree of control over NP size and spatial

positioning, directly comparable to the probe dimensions employed. These results show how SECCM can serve as a powerful tool for the study of fundamental nucleation and growth processes and a practical approach for the fabrication of well-ordered, nanostructured systems.

Experimental Methods

Chemicals and Materials. $AgNO_3$ (99.95%, Salt Lake Metals) and KNO_3 (ACS Reagent Grade, EM Science) were obtained from the indicated sources and used without further purification. Ag wire (0.25 mm diameter, 99.99%, Goodfellow) was used as received in the construction of SECCM probes. ITO substrates (22 x 22 mm, #1.5, 30-60 Ω $sq.^{-1}$, SPI) were cleaned via sequential sonication in deionized water, isopropanol, and again in deionized water for 10 min each before being utilized in electrodeposition experiments.

Fabrication and Characterization of SECCM Probes. Single barrel SECCM probes were fabricated from quartz capillary tubes (1.2 mm OD, 0.9 mm ID, Sutter) using a laser-assisted pipet puller (Sutter P-2000). The following two-line program was employed for the fabrication of all probes used in these studies: HEAT = 740, FIL = 4, VEL = 30, DEL = 150, PULL = 35 / HEAT = 710, FIL = 3, VEL = 30, DEL = 135, PULL = 125. A fabricated pipet was filled with an electrolyte solution of interest using a glass syringe (Microfil 34G) and a Ag wire was inserted in the open end of the pipet to yield a complete probe. Pipet dimensions were characterized using scanning electron microscopy (JEOL 5800 LV SEM, 5 kV accelerating voltage).

SECCM Electrodeposition Procedure. SECCM electrodeposition experiments were carried out using a home-built SECCM apparatus which has been described in detail elsewhere.[70–73] An indium tin oxide (ITO) substrate served as the working electrode. SECCM probes were mounted to a 3-axis piezo system (PI Nanocube 611.3S and E-727 controller). During one electrodeposition

cycle, an initial potential (E_1) was applied between the ITO substrate and the Ag QRCE in the SECCM probe using an electrometer (Dagan CHEM-CLAMP) while the probe was moved towards the ITO surface (2 um/s). The current flowing in the system was monitored during the approach procedure and probe-sample contact was recognized as a sudden spike in the current. Probe movement was then ceased and a cathodic deposition potential (E_2) was then applied to drive NP formation, recording the current flowing during the deposition process. Once a desired total cathodic charge was passed, the probe was retracted and move to a new sample location. This procedure was controlled using custom Labview software and a data acquisition interface (National Instruments cDAQ-9174).

Characterization of Nanoparticle Arrays. After electrodeposition, the NP arrays were characterized through a combination of scanning electron microscopy (FEI Quanta FEG 450, 10 keV) and atomic force microscopy (AFM). AFM imaging was carried out using a Cypher ES AFM in tapping mode with standard probes (Nanosensors, PPP-NCHR-20, n-Si, 0.01–0.02 Ω cm). Dark field microscopy images were acquired using a custom optical setup employing a long working distance microscope objective (Olympus LMPlanFL N 50x, 0.5 NA), a broadband light source (Energetiq EQ-99X), and a microscope eyepiece camera (OMAX A3RDF50/A3590U).

ASSOCIATED CONTENT

Supporting Information. The following files are available free of charge.

Details on numerical simulations, probe characterization, and data analysis (PDF)

AUTHOR INFORMATION

Corresponding Author

*caleb.hill@uwyo.edu

Author Contributions

The manuscript was written through contributions of all authors. All authors have given approval to the final version of the manuscript.

ACKNOWLEDGMENT

The authors acknowledge generous support for this work from the National Science Foundation (CHE-2045593 and OIA-2119237) and the University of Wyoming School of Energy Resources.

ABBREVIATIONS

NP, nanoparticle; SECCM, scanning electrochemical cell microscopy; ITO, indium tin oxide.

REFERENCES

(1) Mulvaney, P. Surface Plasmon Spectroscopy of Nanosized Metal Particles. *Langmuir* **1996**, *12* (3), 788–800. https://doi.org/10.1021/la9502711.

(2) Han, S. H.; Liu, H. M.; Bai, J.; Tian, X. L.; Xia, B. Y.; Zeng, J. H.; Jiang, J. X.; Chen, Y. Platinum-Silver Alloy Nanoballoon Nanoassemblies with Super Catalytic Activity for the Formate Electrooxidation. *ACS Appl Energy Mater* **2018**, *1* (3), 1252–1258. https://doi.org/10.1021/acsaem.8b00004.

(3) Saito, K.; Tatsuma, T. Control of Asymmetric Scattering Behavior of Plasmonic Nanoparticle Ensembles. *ACS Photonics* **2016**, *3* (10), 1782–1786. https://doi.org/10.1021/acsphotonics.6b00547.

(4) Molinnus, D.; Beging, S.; Lowis, C.; Schöning, M. J. Towards a Multi-Enzyme Capacitive Field-Effect Biosensor by Comparative Study of Drop-Coating and Nano-Spotting Technique. *Sensors* **2020**, *20* (17), 4924. https://doi.org/10.3390/s20174924.

(5) Ahmad, R.; Wolfbeis, O. S.; Hahn, Y.-B.; Alshareef, H. N.; Torsi, L.; Salama, K. N. Deposition of Nanomaterials: A Crucial Step in Biosensor Fabrication. *Mater Today Commun* **2018**, *17* (July), 289–321. https://doi.org/10.1016/j.mtcomm.2018.09.024.

(6) Beging, S.; Leinhos, M.; Jablonski, M.; Poghossian, A.; Schöning, M. J. Studying the Spatially Resolved Immobilisation of Enzymes on a Capacitive Field-Effect Structure by

Means of Nano-Spotting. *physica status solidi (a)* **2015**, *212* (6), 1353–1358. https://doi.org/10.1002/pssa.201431891.

(7) Tröger, V.; Malik, S.; Sonntag, F.; Schmieder, S. Generation of Ready-to-Use SPR Chips Using Automated Nano-Spotting. *Biomedical Engineering / Biomedizinische Technik* **2012**, *57* (SI-1 Track-E), 589–592. https://doi.org/10.1515/bmt-2012-4251.

(8) Ahmad, R.; Wolfbeis, O. S.; Hahn, Y.-B.; Alshareef, H. N.; Torsi, L.; Salama, K. N. Deposition of Nanomaterials: A Crucial Step in Biosensor Fabrication. *Mater Today Commun* **2018**, *17* (July), 289–321. https://doi.org/10.1016/j.mtcomm.2018.09.024.

(9) Molinnus, D.; Beging, S.; Lowis, C.; Schöning, M. J. Towards a Multi-Enzyme Capacitive Field-Effect Biosensor by Comparative Study of Drop-Coating and Nano-Spotting Technique. *Sensors* **2020**, *20* (17), 4924. https://doi.org/10.3390/s20174924.

(10) Mayer, K. M.; Hafner, J. H. *Localized Surface Plasmon Resonance Sensors*; American Chemical Society, 2011; Vol. 111, pp 3828–3857. https://doi.org/10.1021/cr100313v.

(11) Kelly, K. L.; Coronado, E.; Zhao, L. L.; Schatz, G. C. The Optical Properties of Metal Nanoparticles: The Influence of Size, Shape, and Dielectric Environment. *Journal of Physical Chemistry B* **2003**, *107* (3), 668–677. https://doi.org/10.1021/jp026731y.

(12) Henzie, J.; Andrews, S. C.; Ling, X. Y.; Li, Z.; Yang, P. Oriented Assembly of Polyhedral Plasmonic Nanoparticle Clusters. *Proc Natl Acad Sci U S A* **2013**, *110* (17), 6640–6645. https://doi.org/10.1073/pnas.1218616110.

(13) Yonzon, C. R.; Jeoung, E.; Zou, S.; Schatz, G. C.; Mrksich, M.; Van Duyne, R. P. A Comparative Analysis of Localized and Propagating Surface Plasmon Resonance Sensors: The Binding of Concanavalin A to a Monosaccharide Functionalized Self-Assembled Monolayer. *J Am Chem Soc* **2004**, *126* (39), 12669–12676. https://doi.org/10.1021/JA047118Q/ASSET/IMAGES/JA047118Q.SOCIAL.JPEG_V03.

(14) Zhang, H.; Kinnear, C.; Mulvaney, P. Fabrication of Single-Nanocrystal Arrays. *Advanced Materials* **2019**, 1904551. https://doi.org/10.1002/adma.201904551.

(15) Gargiulo, J.; Cerrota, S.; Cortés, E.; Violi, I. L.; Stefani, F. D. Connecting Metallic Nanoparticles by Optical Printing. *Nano Lett* **2016**, *16* (2), 1224–1229. https://doi.org/10.1021/acs.nanolett.5b04542.

(16) Akinoglu, E. M.; Morfa, A. J.; Giersig, M. Understanding Anisotropic Plasma Etching of Two-Dimensional Polystyrene Opals for Advanced Materials Fabrication. *Langmuir* **2014**, *30* (41), 12354–12361. https://doi.org/10.1021/la500003u.

(17) Ding, B.; Wu, H.; Xu, W.; Zhao, Z.; Liu, Y.; Yu, H.; Yan, H. Interconnecting Gold Islands with DNA Origami Nanotubes. *Nano Lett* **2010**, *10* (12), 5065–5069. https://doi.org/10.1021/nl1033073.

(18) Pearson, A. C.; Pound, E.; Woolley, A. T.; Linford, M. R.; Harb, J. N.; Davis, R. C. Chemical Alignment of DNA Origami to Block Copolymer Patterned Arrays of 5 Nm Gold Nanoparticles. *Nano Lett* **2011**, *11* (5), 1981–1987. https://doi.org/10.1021/nl200306w.

(19) Zhou, X.; Zhou, Y.; Ku, J. C.; Zhang, C.; Mirkin, C. A. Capillary Force-Driven, Large-Area Alignment of Multi-Segmented Nanowires. *ACS Nano* **2014**, *8* (2), 1511–1516. https://doi.org/10.1021/nn405627s.

(20) Hung, A. M.; Micheel, C. M.; Bozano, L. D.; Osterbur, L. W.; Wallraff, G. M.; Cha, J. N. Large-Area Spatially Ordered Arrays of Gold Nanoparticles Directed by Lithographically Confined DNA Origami. *Nat Nanotechnol* **2010**, *5* (2), 121–126. https://doi.org/10.1038/nnano.2009.450.

(21) M. George, S. Atomic Layer Deposition: An Overview. *Chem Rev* **2009**, *110* (1), 111–131. https://doi.org/10.1021/cr900056b.

(22) Ritala, M.; Leskelä, M. Atomic Layer Deposition. *Handbook of Thin Films* **2002**, 103–159. https://doi.org/10.1016/B978-012512908-4/50005-9.

(23) Johnson, R. W.; Hultqvist, A.; Bent, S. F. A Brief Review of Atomic Layer Deposition: From Fundamentals to Applications. *Materials Today* **2014**, *17* (5), 236–246. https://doi.org/10.1016/J.MATTOD.2014.04.026.

(24) Xia, Y.; Whitesides, G. M. Soft Lithography. *Angewandte Chemie - International Edition* **1998**, *37* (5), 550–575. https://doi.org/10.1002/(sici)1521-3773(19980316)37:5<550::aid-anie550>3.3.co;2-7.

(25) W. Odom, T.; Christopher Love, J.; B. Wolfe, D.; E. Paul, K.; M. Whitesides, G. Improved Pattern Transfer in Soft Lithography Using Composite Stamps. *Langmuir* **2002**, *18* (13), 5314–5320. https://doi.org/10.1021/la020169l.

(26) Kosiorek, A.; Kandulski, W.; Chudzinski, P.; Kempa, K.; Giersig, M. Shadow Nanosphere Lithography: Simulation and Experiment. *Nano Lett* **2004**, *4* (7), 1359–1363. https://doi.org/10.1021/nl049361t.

(27) Schift, H. Nanoimprint Lithography: An Old Story in Modern Times? A Review. *Journal of Vacuum Science and Technology B: Microelectronics and Nanometer Structures* **2008**, *26* (2), 458–480. https://doi.org/10.1116/1.2890972.

(28) Kooy, N.; Mohamed, K.; Pin, L. T.; Guan, O. S. A Review of Roll-to-Roll Nanoimprint Lithography. *Nanoscale Res Lett* **2014**, *9* (1), 1–13. https://doi.org/10.1186/1556-276X-9-320.

(29) Krauss, P. R.; Chou, S. Y. Nano-Compact Disks with 400 Gbit/In2 Storage Density Fabricated Using Nanoimprint Lithography and Read with Proximal Probe. *Appl Phys Lett* **1997**, *71* (21), 3174–3176. https://doi.org/10.1063/1.120280.

(30) Wu, D.; S. Rajput, N.; Luo, X. Nanoimprint Lithography - the Past, the Present and the Future. *Curr Nanosci* **2016**, *12* (6), 712–724. https://doi.org/10.2174/1573413712666160530120432.

(31) Garcia, R.; Knoll, A. W.; Riedo, E. Advanced Scanning Probe Lithography. *Nat Nanotechnol* **2014**, *9* (8), 577–587. https://doi.org/10.1038/nnano.2014.157.

(32) Ebejer, N.; Güell, A. G.; Lai, S. C. S.; McKelvey, K.; Snowden, M. E.; Unwin, P. R. Scanning Electrochemical Cell Microscopy: A Versatile Technique for Nanoscale Electrochemistry and Functional Imaging. *Annual review of analytical chemistry* **2013**, *6* (1), 329–351. https://doi.org/10.1146/annurev-anchem-062012-092650.

(33) Daviddi, E.; Gonos, K. L.; Colburn, A. W.; Bentley, C. L.; Unwin, P. R. Scanning Electrochemical Cell Microscopy (SECCM) Chronopotentiometry: Development and Applications in Electroanalysis and Electrocatalysis. *Anal Chem* **2019**, *91* (14), 9229–9237. https://doi.org/10.1021/acs.analchem.9b02091.

(34) Wahab, O. J.; Kang, M.; Unwin, P. R. Scanning Electrochemical Cell Microscopy: A Natural Technique for Single Entity Electrochemistry. *Curr Opin Electrochem* **2020**, *22*, 120–128. https://doi.org/10.1016/j.coelec.2020.04.018.

(35) Lai, S. C. S.; Lazenby, R. A.; Kirkman, P. M.; Unwin, P. R. Nucleation, Aggregative Growth and Detachment of Metal Nanoparticles during Electrodeposition at Electrode Surfaces. *Chem Sci* **2015**, *6* (2), 1126–1138. https://doi.org/10.1039/C4SC02792B.

(36) Siepser, N. P.; Choi, M.-H.; Alden, S. E.; Baker, L. A. Single-Entity Electrocatalysis at Electrode Ensembles Prepared by Template Synthesis. *J Electrochem Soc* **2021**, *168* (12), 126526. https://doi.org/10.1149/1945-7111/ac44b8.

(37) Jeong, S.; Choi, M.-H.; Jagdale, G. S.; Zhong, Y.; Siepser, N. P.; Wang, Y.; Zhan, X.; Baker, L. A.; Ye, X. Unraveling the Structural Sensitivity of CO 2 Electroreduction at Facet-Defined Nanocrystals via Correlative Single-Entity and Macroelectrode Measurements. *J Am Chem Soc* **2022**, *144* (28), 12673–12680. https://doi.org/10.1021/jacs.2c02001.

(38) Bentley, C. L.; Edmondson, J.; Meloni, G. N.; Perry, D.; Shkirskiy, V.; Unwin, P. R. Nanoscale Electrochemical Mapping. *Anal Chem* **2019**, *91* (1), 84–108. https://doi.org/10.1021/acs.analchem.8b05235.

(39) Alden, S. E.; Siepser, N. P.; Patterson, J. A.; Jagdale, G. S.; Choi, M.; Baker, L. A. Array Microcell Method (AMCM) for Serial Electroanalysis. *ChemElectroChem* **2020**, *7* (5), 1084–1091. https://doi.org/10.1002/celc.201901976.

(40) Choi, M.; Siepser, N. P.; Jeong, S.; Wang, Y.; Jagdale, G.; Ye, X.; Baker, L. A. Probing Single-Particle Electrocatalytic Activity at Facet-Controlled Gold Nanocrystals. *Nano Lett* **2020**, *20* (2), 1233–1239. https://doi.org/10.1021/acs.nanolett.9b04640.

(41) Bentley, C. L.; Kang, M.; Unwin, P. R. Nanoscale Structure Dynamics within Electrocatalytic Materials. *J Am Chem Soc* **2017**, *139* (46), 16813–16821. https://doi.org/10.1021/jacs.7b09355.

(42) Bentley, C. L.; Kang, M.; Unwin, P. R. Nanoscale Surface Structure–Activity in Electrochemistry and Electrocatalysis. *J Am Chem Soc* **2019**, *141* (6), 2179–2193. https://doi.org/10.1021/jacs.8b09828.

(43) Li, M.; Ye, K.-H.; Qiu, W.; Wang, Y.; Ren, H. Heterogeneity between and within Single Hematite Nanorods as Electrocatalysts for Oxygen Evolution Reaction. *J Am Chem Soc* **2022**, *144* (12), 5247–5252. https://doi.org/10.1021/jacs.2c00506.

(44) Mariano, R. G.; McKelvey, K.; White, H. S.; Kanan, M. W. Selective Increase in CO2 Electroreduction Activity at Grain-Boundary Surface Terminations. *Science (1979)* **2017**, *358* (6367), 1187–1192. https://doi.org/10.1126/science.aao3691.

(45) Wang, Y.; Li, M.; Gordon, E.; Ye, Z.; Ren, H. Nanoscale Colocalized Electrochemical and Structural Mapping of Metal Dissolution Reaction. *Anal Chem* **2022**, *94* (25), 9058–9064. https://doi.org/10.1021/ACS.ANALCHEM.2C01283/SUPPL_FILE/AC2C01283_SI_003.AVI.

(46) Li, M.; Wang, Y.; Blount, B.; Gordon, E.; Muñoz-Castañeda, J. A.; Ye, Z.; Ren, H. Stochastic Local Breakdown of Oxide Film on Ni from Identical-Location Imaging: One Single Site at a Time. *Nano Lett* **2022**, *22* (15), 6313–6319. https://doi.org/10.1021/acs.nanolett.2c02018.

(47) Tolbert, C. L.; Hill, C. M. Electrochemically Probing Exciton Transport in Monolayers of Two-Dimensional Semiconductors. *Faraday Discuss* **2022**, *233*, 163–174. https://doi.org/10.1039/D1FD00052G.

(48) Strange, L. E.; Yadav, J.; Garg, S.; Shinde, P. S.; Hill, J. W.; Hill, C. M.; Kung, P.; Pan, S. Investigating the Redox Properties of Two-Dimensional MoS 2 Using Photoluminescence Spectroelectrochemistry and Scanning Electrochemical Cell Microscopy. *J Phys Chem Lett* **2020**, *11* (9), 3488–3494. https://doi.org/10.1021/acs.jpclett.0c00769.

(49) Hill, J. W.; Hill, C. M. Directly Mapping Photoelectrochemical Behavior within Individual Transition Metal Dichalcogenide Nanosheets. *Nano Lett* **2019**, *19* (8), 5710–5716. https://doi.org/10.1021/acs.nanolett.9b02336.

(50) Hill, J. W.; Hill, C. M. Directly Visualizing Carrier Transport and Recombination at Individual Defects within 2D Semiconductors. *Chem Sci* **2021**, *12* (14), 5102–5112. https://doi.org/10.1039/d0sc07033e.

(51) Hill, J. W.; Fu, Z.; Tian, J.; Hill, C. M. Locally Engineering and Interrogating the Photoelectrochemical Behavior of Defects in Transition Metal Dichalcogenides. *The Journal of Physical Chemistry C* **2020**, *124* (31), 17141–17149. https://doi.org/10.1021/acs.jpcc.0c05235.

(52) Fu, Z.; Hill, J. W.; Parkinson, B.; Hill, C. M.; Tian, J. Layer and Material-Type Dependent Photoresponse in WSe 2 /WS 2 Vertical Heterostructures. *2d Mater* **2022**, *9* (1), 015022. https://doi.org/10.1088/2053-1583/ac3c9c.

(53) Bentley, C. L.; Kang, M.; Bukola, S.; Creager, S. E.; Unwin, P. R. High-Resolution Ion-Flux Imaging of Proton Transport through Graphene|Nafion Membranes. *ACS Nano* **2022**, *16* (4), 5233–5245. https://doi.org/10.1021/ACSNANO.1C05872/ASSET/IMAGES/LARGE/NN1C05872_0005.JPEG.

(54) McPherson, I. J.; Peruffo, M.; Unwin, P. R. Role of Mass Transport in the Deposition, Growth, and Transformation of Calcium Carbonate on Surfaces at High Supersaturation. *Cryst Growth Des* **2022**, *22* (8), 4721–4729. https://doi.org/10.1021/acs.cgd.1c01505.

(55) Scharifker, B.; Hills, G. Theoretical and Experimental Studies of Multiple Nucleation. *Electrochim Acta* **1983**, *28* (7), 879–889. https://doi.org/10.1016/0013-4686(83)85163-9.

(56) Fletcher, S.; Halliday, C. S.; Gates, D.; Westcott, M.; Lwin, T.; Nelson, G. The Response of Some Nucleation/Growth Processes to Triangular Scans of Potential. *J Electroanal Chem Interfacial Electrochem* **1983**, *159* (2), 267–285. https://doi.org/10.1016/S0022-0728(83)80627-5.

(57) Polte, J. Fundamental Growth Principles of Colloidal Metal Nanoparticles – a New Perspective. *CrystEngComm* **2015**, *17* (36), 6809–6830. https://doi.org/10.1039/C5CE01014D.

(58) Fleischmann, M.; Li, L. J.; Peter, L. M. Molecular Level Measurements of the Kinetics of Nucleation of α-PbO2 on Carbon Microelectrodes. *Electrochim Acta* **1989**, *34* (3), 475–483. https://doi.org/10.1016/0013-4686(89)87027-6.

(59) Chen, S.; Kucernak, A. Electrodeposition of Platinum on Nanometer-Sized Carbon Electrodes. *J Phys Chem B* **2003**, *107* (33), 8392–8402. https://doi.org/10.1021/jp0348934.

(60) Chen, S.; Kucernak, A. Electrocatalysis under Conditions of High Mass Transport: Investigation of Hydrogen Oxidation on Single Submicron Pt Particles Supported on Carbon. *J Phys Chem B* **2004**, *108* (37), 13984–13994. https://doi.org/10.1021/jp048641u.

(61) Chen, S.; Kucernak, A. Electrocatalysis under Conditions of High Mass Transport Rate: Oxygen Reduction on Single Submicrometer-Sized Pt Particles Supported on Carbon. *Journal of Physical Chemistry B* **2004**, *108* (10), 3262–3276. https://doi.org/10.1021/jp036831j.

(62) Glasscott, M. W.; Hill, C. M.; Dick, J. E. Quantifying Growth Kinetics of Single Nanoparticles in Sub-Femtoliter Reactors. *The Journal of Physical Chemistry C* **2020**, *124* (26), 14380–14389. https://doi.org/10.1021/acs.jpcc.0c03518.

(63) Weber, M. L.; Litz, J. P.; Masiello, D. J.; Willets, K. A. Super-Resolution Imaging Reveals a Difference between SERS and Luminescence Centroids. *ACS Nano* **2012**, *6* (2), 1839–1848. https://doi.org/10.1021/nn205080q.

(64) Titus, E. J.; Willets, K. A. Accuracy of Superlocalization Imaging Using Gaussian and Dipole Emission Point-Spread Functions for Modeling Gold Nanorod Luminescence. *ACS Nano* **2013**, *7* (7), 6258–6267. https://doi.org/10.1021/nn4022845.

(65) Titus, E. J.; Willets, K. A. Superlocalization Surface-Enhanced Raman Scattering Microscopy: Comparing Point Spread Function Models in the Ensemble and Single-Molecule Limits. *ACS Nano* **2013**, *7* (9), 8284–8294. https://doi.org/10.1021/nn403891t.

(66) Stranahan, S. M.; Willets, K. A. Super-Resolution Optical Imaging of Single-Molecule SERS Hot Spots. *Nano Lett* **2010**, *10* (9), 3777–3784. https://doi.org/10.1021/nl102559d.

(67) Despic, A. R.; Bockris, J. O. M. Kinetics of the Deposition and Dissolution of Silver. *J Chem Phys* **1960**, *32* (2), 389–402. https://doi.org/10.1063/1.1730706.

(68) Glasscott, M. W.; Hill, C. M.; Dick, J. E. Quantifying Growth Kinetics of Single Nanoparticles in Sub-Femtoliter Reactors. *The Journal of Physical Chemistry C* **2020**, *124* (26), 14380–14389. https://doi.org/10.1021/acs.jpcc.0c03518.

(69) McPherson, I. J.; Peruffo, M.; Unwin, P. R. Role of Mass Transport in the Deposition, Growth, and Transformation of Calcium Carbonate on Surfaces at High Supersaturation. *Cryst Growth Des* **2022**, *22* (8), 4721–4729. https://doi.org/10.1021/acs.cgd.1c01505.

(70) Walmsley, J. D.; Hill, J. W.; Saha, P.; Hill, C. M. Probing Electrocatalytic CO_2 Reduction at Individual Cu Nanostructures via Optically Targeted Electrochemical Cell Microscopy. *J Anal Test* **2019**, *3* (2), 140–149. https://doi.org/10.1007/s41664-019-00090-3.

(71) Saha, P.; Hill, J. W.; Walmsley, J. D.; Hill, C. M. Probing Electrocatalysis at Individual Au Nanorods via Correlated Optical and Electrochemical Measurements. *Anal Chem* **2018**, *90* (21), 12832–12839. https://doi.org/10.1021/acs.analchem.8b03360.

(72) Saha, P.; Rahman, Md. M.; Hill, C. M. Borohydride Oxidation Electrocatalysis at Individual, Shape-controlled Au Nanoparticles. *Electrochemical Science Advances* **2021**. https://doi.org/10.1002/elsa.202100120.

(73) Maley, M.; Hill, J. W.; Saha, P.; Walmsley, J. D.; Hill, C. M. The Role of Heating in the Electrochemical Response of Plasmonic Nanostructures under Illumination. *Journal of Physical Chemistry C* **2019**, *123* (19), 12390–12399. https://doi.org/10.1021/ACS.JPCC.9B01479/SUPPL_FILE/JP9B01479_SI_002.PDF.

TOC Graphic